Journal of Solid State Chemistry 183 (2010) 2826–2834

Contents lists available at ScienceDirect

Journal of Solid State Chemistry

journal homepage: www.elsevier.com/locate/jssc

Stability of $Ba(Zr,Pr,Y)O_{3-\delta}$ materials for potential application in electrochemical devices

I. Antunes [a], G.C. Mather [b], J.R. Frade [a], J. Gracio [c], D.P. Fagg [c,*]

[a] Department of Ceramics and Glass Engineering, CICECO, University of Aveiro, 3810 193 Aveiro, Portugal
[b] Institute of Ceramics and Glass, CSIC, Cantoblanco, 28049 Madrid, Spain
[c] Nanotechnology Research Division, Centre of Mechanical Technology and Automation, University of Aveiro, 3810 193 Aveiro, Portugal

ARTICLE INFO

Article history:
Received 25 June 2010
Received in revised form
14 September 2010
Accepted 16 September 2010
Available online 21 September 2010

Keywords:
Mixed conductor
Solid oxide fuel cell
Proton conductor
Perovskite
$BaZrO_3$
$BaPrO_3$
Cathode

ABSTRACT

$Ba(Pr_{1-x}Zr_x)_{1-y}Y_yO_{3-\delta}$ materials were obtained by a two-step process of mechanical activation followed by annealing at 1250 °C. Guidelines for correlations between structure and composition, and their role on stability were characterised as a function of atmosphere, with special emphasis on degradation by carbonation in CO_2-rich atmospheres, or upon redox changes. The role of humidity on these degradation processes was also analysed by taking into account differences between wet and dry atmospheres with regards to the onset of secondary phases and structural changes. Thermodynamic calculations were used to predict 2-phase and 3-phase equilibria in contact with CO_2-rich atmospheres and to obtain corresponding stability diagrams. The thermodynamic calculations were also used as guidelines for the progress of carbonation in isothermal conditions, and also with variable temperature, namely on cooling carbonate free materials from high temperatures, or on re-heating under CO_2.

1. Introduction

The most well-known intermediate temperature proton-conducting materials are perovskite oxides (ABO_3) with large basic A cations (e.g. Ba, Sr) and tetravalent *B* cations (e.g. Zr, Ce). Such perovskites incorporate protons in the presence of H_2O when doped with a lower valence cation on the *B*-site, with hydroxyl groups filling the oxygen vacancies and protons forming additional hydroxyl groups with lattice oxygens. Although these materials have received extensive interest as potential electrolytes, the study of homogeneous mixed proton and electron conductors, where mixed conductivity is introduced in a single phase, is still in its infancy. This class of materials would find application as electrodes in proton ceramic fuel cells (PCFC) or as hydrogen separation membranes. One candidate system is $Ba(Pr,R)O_{3-\delta}$ (R=rare earth) where the presence of mixed valence Pr introduces electronic conductivity [1,2]. However, reports on the electrical transport data of this system have been rather contradictory [1–8]. The most recent works show $Ba(Pr,R)O_{3-\delta}$ to be a predominant electronic conductor, offering only minimal proton conductivity, which is susceptible to decomposition in both wet and dry reducing conditions, moist oxidising conditions, CO_2-containing atmospheres, and also on high-temperature processing [4–6]. This high level of instability has led several authors to render these materials as not useful for SOFC purposes [5,6].

The cerium analogue, $Ba(Ce,R)O_{3-\delta}$, also exhibits poor stability, rapidly decomposing in H_2O- and CO_2-containing atmospheres [9,10]. However, a radical improvement in stability has been achieved by the partial substitution of cerium for zirconium [11], generating considerable interest in this system as a promising electrolyte material. Recently, the same strategy was suggested for the improvement of stability in $Ba(Pr,Gd)O_{3-\delta}$ compounds. Magrasó et al. [12] investigated the solid solution $BaZr_xPr_{0.7-x}Gd_{0.3}O_{3-\delta}$ and demonstrated enhanced stability at high Zr contents; for example, materials with values of $x \geq 0.5$ appeared stable under annealing in 5% H_2/Ar, while for $x \geq 0.4$ improved stability under wet Ar was reported.

It is widely documented that the stability of the perovskite phase is related to the tolerance factor

$$t = \frac{r_A + r_O}{\sqrt{2}(r_B + r_O)} \quad (1)$$

where r_A, r_B, and r_O are the ionic radii of the *A*, *B*, and oxide ions, respectively. Compositions that are closer to the ideal cubic form (t=1) present the higher stabilities [13]. Indeed the work of Magrasó et al. [12] follows this guideline as the perovskite phase was observed to offer improved stability when progressing from orthorhombically distorted to cubic with increase in the Zr content. This orthorhombic lattice distortion arises because the

* Corresponding author. Fax: +351 234 370 953.
E-mail address: duncan@ua.pt (D.P. Fagg).

0022-4596/$ - see front matter © 2010 Elsevier Inc. All rights reserved.
doi:10.1016/j.jssc.2010.09.021

average *B*-site ionic radius becomes too large for the ideal $Pm\bar{3}m$ aristotype with increase in the Pr concentration. For the investigated solid solution, such "over sizing" of the *B*-site cation would also be compounded by the high concentration of the large gadolinium dopant ion. In support of this, microstructural investigations by Magrasó et al. revealed gadolinium segregation at high sintering temperatures. Hence, further improvements in stability of $BaPrO_{3-\delta}$-based materials are still required before they can be implemented in electrochemical devices. In the current article, we aim to improve on the stability of current literature materials by reducing the acceptor dopant concentration and selecting a smaller dopant (yttrium). The compositions studied are $Ba(Pr_{1-x}Zr_x)_{0.9}Y_{0.1}O_{3-\delta}$ and $Ba(Pr_{1-x}Zr_x)_{0.8}Y_{0.2}O_{3-\delta}$ for $0 \le x \le 1$. The relations between stability, dopant levels, dopant size, and observed crystallographic symmetry will be discussed, with the aim of producing guidelines that can facilitate the design of stable materials based on $BaPrO_3$ for potential applications.

2. Experimental

Powders of $Ba(Pr,Zr,Y)O_{3-\delta}$ were prepared by two techniques: (1) solid-state synthesis starting from stoichiometric mixtures of $BaCO_3$ (Aldrich $>99\%$) and the respective metal oxides Y_2O_3 (Hermann C. Stark, calcined 950 °C, 1 h), Pr_6O_{11} (Aldrich $>99.9\%$), and ZrO_2 (Riedel-de-Haen $>99\%$) with repeated firing (1500 °C, 5 h) and regrinding steps; (2) a two-step process of mechanical activation followed by annealing (1250 °C, 5 h), using stoichiometric quantities of 95% purity), Pr_6O_{11} (Aldrich $>99.9\%$), $(ZrO_2)_{0.97}(Y_2O_3)_{0.03}$ (TOSOH Co,), and Y_2O_3 (Hermann C. Stark), calcined at 950 °C for 1 h. The commercial powder of barium peroxide was found to be a mixture of 95 mol% BaO_2 with 5 mol% $BaCO_3$, the exact quantities of which were calculated by thermogravimetric analysis using a SETARAM TG-DTA/DSC Labsys Instrument with a 1600 °C rod by complete carbonation of a sample in flowing CO_2. Mechanical activation was performed in a planetary ball mill (Retsch PM200) with constant planetary rotation of 650 rpm using tetragonal zirconia balls and vials. The ball-to-powder weight ratio was ~10:1. Excess heating was avoided by milling for periods of 5 min with a subsequent pause for the same period of time. After each interruption, the direction of rotation was reversed. No special atmospheres were used during grinding. Stability in flowing, dry CO_2 was assessed by thermogravimetric analysis using the SETARAM instrument with a heating rate of 1 °C/min–1300 °C. For this, samples were preliminarily heated at 5 °C/min in dry argon to 1300 °C to remove residual hydration and any minor initial traces of $BaCO_3$, and cooled under the same atmosphere. Stability was further assessed by post-operation examination by X-ray diffraction (XRD) of samples annealed for 12 h at 600 °C in wet and dry oxygen, carbon dioxide and 10% hydrogen/nitrogen atmospheres.

Rietveld refinement of powder XRD data was performed with the FULLPROF programme [14] in order to determine unit-cell parameters. Diffraction data were collected with a Rigaku Geigerflex D/Max B diffractometer using Cu$K\alpha$ radiation over the range $15^\circ \le 2\theta \le 115^\circ$ with a stepwidth of 0.02° and scan rate of 6 s/step.

3. Results and discussion

3.1. Phase preparation

Despite repeated cycles of high-temperature firing and regrinding, phase purity was not obtained by the solid-state preparation technique. The X-ray powder diffraction patterns of the system $Ba(Pr_{1-x}Zr_x)_{0.8}Y_{0.2}O_{3-\delta}$, Fig. 1, exhibit broad asymmetric peak shapes, suggesting the presence of inhomogenities, and distinct secondary phases at high Zr-contents, corresponding to a secondary perovskite phase of smaller lattice parameter. Mechanosynthesis has been shown to be highly efficient for processing homogeneous, nanometric size powders of $BaZrO_3$ materials at room temperature with low $BaCO_3$ contents [15]. For this reason a similar preparation route was attempted in the current work. High speed milling without further treatment was insufficient for synthesising a single-phase perovskite, forming instead a mixture of the perovskite phase and PrO_2. In contrast, samples mechanically activated for 300 min and annealed at 1250 °C for 5 h show pure phases with well-defined peak shapes suggesting good homogeneity (Fig. 2a). Single-phase perovskite materials can be obtained for all values of x for the two studied systems, $Ba(Pr_{1-x}Zr_x)_{0.9}Y_{0.1}O_{3-\delta}$ and $Ba(Pr_{1-x}Zr_x)_{0.8}Y_{0.2}O_{3-\delta}$; XRD powder patterns are shown in Fig. 2b for the latter system.

3.2. Structural characterisation

Perovskites very often exhibit a number of symmetry changes with increase in tolerance factor, which can occur on increasing temperature or with composition in a solid-solution range. $A^{2+}B^{4+}O_3$ perovskites commonly display the sequence $Pbnm \rightarrow Ibmm \rightarrow I4/mcm \rightarrow Pm\bar{3}m$ on the pathway from orthorhombic to cubic symmetry [16,17]. Other similar sequences have also been reported, with $R\bar{3}c$ observed prior to cubic symmetry for $BaCeO_3$, $BaPrO_3$, and $BaPr_{0.9}Y_{0.1}O_{3-\delta}$ [18,8]. The transitions occur on the progressive loss of tilting of layers of the BO_6 octahedra around the four-fold axes of the cubic aristotype [19]. The tilting can be either in-phase, if the rotations of layers of successive octahedra along an axis are equal, or anti-phase if the tilting is in the opposite sense to the adjacent layers of octahedra. Reaney and coworkers [20,21] have shown a correlation between the tilting characteristics and the tolerance factor. At room temperature, perovskites with tolerance factor in the range $0.985 < t < 1.06$ are associated with untilted cubic structures ($Pm\bar{3}m$). In the range $0.964 < t < 0.985$, anti-phase tilting only (*Ibmm*, $R\bar{3}c$, or $I4/mcm$) is usually exhibited, whereas for $t < 0.964$, both in-phase and anti-phase tilting occurs, with structures in this regime most commonly crystallising in the *Pbnm* space group (alternative setting of *Pnma*). The relations between tilt system and space group have been outlined by Howard and Stokes [22]. The in-phase and anti-phase tilts are associated with movements of the oxygen positions, which are often quite subtle, giving rise to *M*-point and *X*-point superlattice reflections of the cubic aristotype [23]. These reflections are

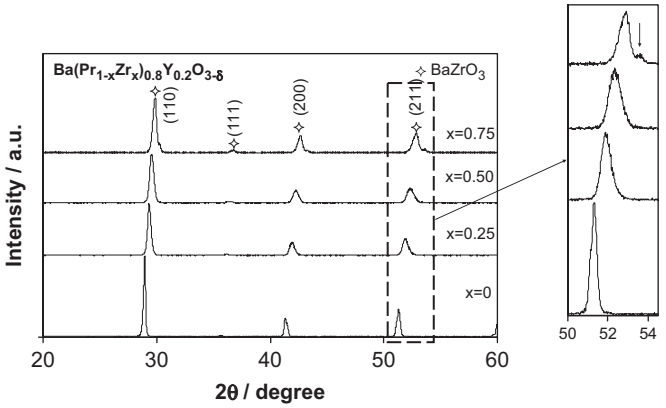

Fig. 1. X-ray diffraction pattern of the $Ba(Pr_{1-x}Zr_x)_{0.8}Y_{0.2}O_{3-\delta}$ system prepared by solid-state synthesis, after a second sintering at 1500 °C, highlighting broad asymmetric peak shapes suggesting the presence of inhomogenities. Arrow indicates secondary phase in composition $x = 0.75$. Stars indicate perovskite phase.

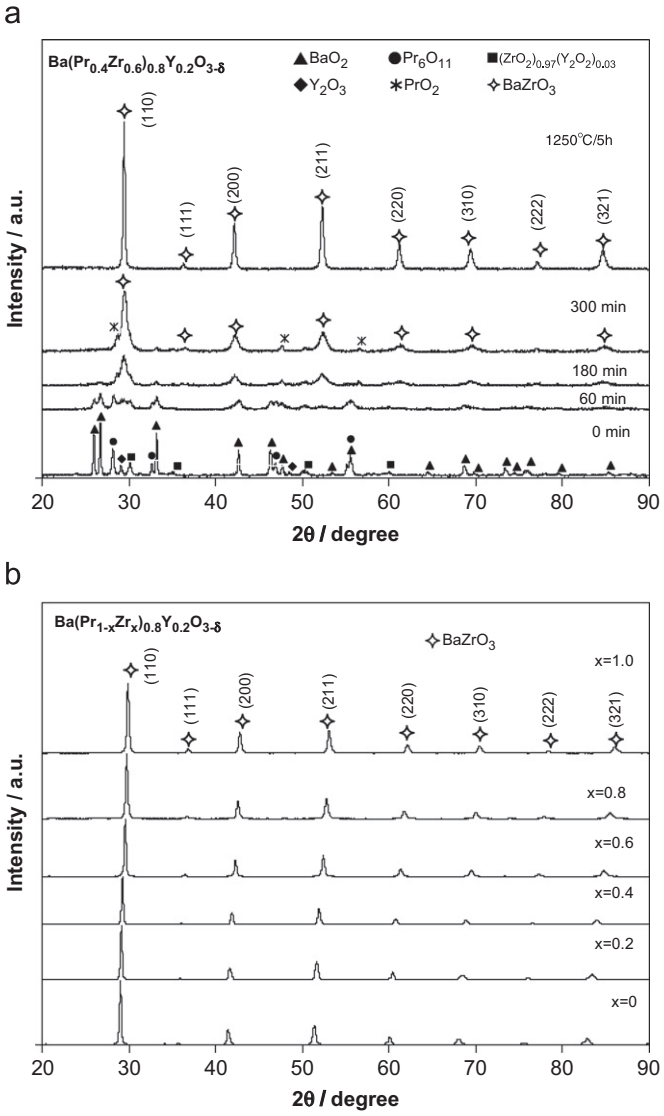

Fig. 2. (a) X-ray diffraction patterns demonstrating the evolution of mechanical activation with milling time and formation of single-phase $Ba(Pr_{1-x}Zr_x)_{0.8}Y_{0.2}O_{3-\delta}$ perovskite after annealing at 1250 °C for 5 h; note the formation of PrO_2 during mechanical activation. (b) X-ray diffraction patterns of the $Ba(Pr_{1-x}Zr_x)_{0.8}Y_{0.2}O_{3-\delta}$ system prepared by a combination of mechanical activation and annealing at 1250 °C for 5 h. Phase purity is obtained for all values of x. Stars indicate perovskite phase.

typically very weak or imperceptible by X-ray diffraction due to the comparatively low X-ray oxygen scattering factor. In many instances, the precise determination of the space group is debatable, and high resolution neutron powder diffraction or electron diffraction is required to solve the exact structure. Here, we have used Rietveld refinement of X-ray diffraction data to obtain an initial analysis of the structures of the $Ba(Pr_{1-x}Zr_x)_{0.9}Y_{0.1}O_{3-\delta}$ and $Ba(Pr_{1-x}Zr_i)_{0.8}Y_{0.2}O_{3-\delta}$ systems, principally on consideration of the lattice parameters, which can be extracted precisely for the reduced (cubic) aristotype.

Fig. 3a and b show the reduced cell (pseudo-cubic) lattice parameters of the two systems as a function of composition. In both cases there is a decrease in unit-cell parameter with increase in the Zr content, which is consistent with the substitution of Pr^{4+}_{VI} (0.85 Å) with the smaller Zr^{4+}_{VI} cation (0.72 Å) [24]. In the $Ba(Pr_{1-x}Zr_x)_{0.9}Y_{0.1}O_{3-\delta}$ family, indexing and subsequent Rietveld analysis indicates that the symmetry changes from orthorhombic (*Pbnm*) for $x=0$ [8] and $x=0.2$ through tetragonal (*I*4/*mcm*) or rhombohedral ($R\bar{3}c$) for $x=0.04$ and 0.06 to cubic ($x=0.8$ and $x=1.0$). Unfortunately, the X-ray data for the intermediate compositions are not of sufficient resolution for determination of the exact symmetry and space group for the reasons outlined above.

Regions where a certain type of tilting regime may be expected on the basis of tolerance factor [20,21] are also shown in Fig. 3a and b, for a Pr oxidation state of 4+. The evolution of the crystal system with composition correlates well with the tolerance factor guidelines. Interestingly, the tolerance factors of the compositions $x=0.4$ and $x=0.8$ of the $Ba(Pr_{1-x}Zr_x)_{0.9}Y_{0.1}O_{3-\delta}$ family both sit on the borderline between anticipated symmetry transitions. Composition $x=0.4$ with tolerance factor 0.964 lies on the transition between regions of in-phase and anti-phase tilting and anti-phase tilting only, whereas composition $x=0.8$ has a tolerance factor of 0.985, which forms the boundary between zones of anti-phase tilted and untilted structures. This highlights the difficulty of the determination of the exact structure of these two compositions without recourse to more powerful diffraction techniques.

The $Ba(Pr_{1-x}Zr_x)_{0.8}Y_{0.2}O_{3-\delta}$ system displays a similar increase in symmetry and lowering of reduced unit-cell parameter with increase in the Zr content (Fig. 3b). In comparison to the $Ba(Pr_{1-x}Zr_x)_{0.9}Y_{0.1}O_{3-\delta}$ system, the higher Y^{3+} content lowers the tolerance factor with the effect that the orthorhombic crystal system is observed up to a higher Zr content. Again, the indexation and Rietveld analysis are consistent with orthorhombic and cubic symmetries for the end-member phases, which are also the symmetries predicted on the basis of tolerance factor. Orthorhombic symmetry associated with in-phase and anti-phase tilting is also expected for compositions $x=0.2$ and 0.4 on considering their respective tolerance factors; the lattice parameters for these compositions and the end-member phase ($x=0$) were thus obtained on refining in the *Pbnm* space group. With further increase in the Zr content, the observed symmetry changes to tetragonal (or pseudo-tetragonal); accordingly the lattice parameters for compositions $x=0.06$ and 0.08 were determined on refinement in *I*4/*mcm*. This space group is associated with anti-phase tilting only, which is to be expected from the corresponding tolerance factors (Fig. 3(b)). The change in unit-cell metric from $c/a<1$ in $x=0.6$ to $c/a>1$ for $x=0.8$ which is exhibited by $Ba(Pr_{1-x}Zr_x)_{0.8}Y_{0.2}O_{3-\delta}$ (Fig. 3b) has also been observed on heating $SrZrO_3$ [17]. In this case, the change could be attributed to a transition from pseudo-tetragonal (*Ibmm*) to tetragonal (*I*4/*mcm*) symmetry. Perhaps a similar transition occurs as a function of composition in the $Ba(Pr_{1-x}Zr_x)_{0.8}Y_{0.2}O_{3-\delta}$ system. It is expected that further structural details will be given in future communications.

3.3. Stability studies

3.3.1. Dry and wet O_2

The stability of the perovskite phase is commonly related to the tolerance factor [13]; hence, the stability of the title materials on annealing in various gas atmospheres at 600 °C for 12 h is displayed collectively with the structural information in Fig. 3a and b. Stability, for the current purposes, is defined to be the absence of secondary phases on post-op examination at the resolution of X-ray diffraction (XRD). Samples that meet with this criterion are represented by bullet points in Fig. 3a and b for each gas environment. In wet and dry oxygen environments, $BaPr_{1-x}Y_xO_{3-\delta}$ samples partially decompose to form praseodymium oxide and barium carbonate in addition to the perovskite phase. The presence of $BaCO_3$ is probably due to rapid reaction between BaO and CO_2 after removal of the sample from the furnace. Signs of hydroxide formation, as documented for

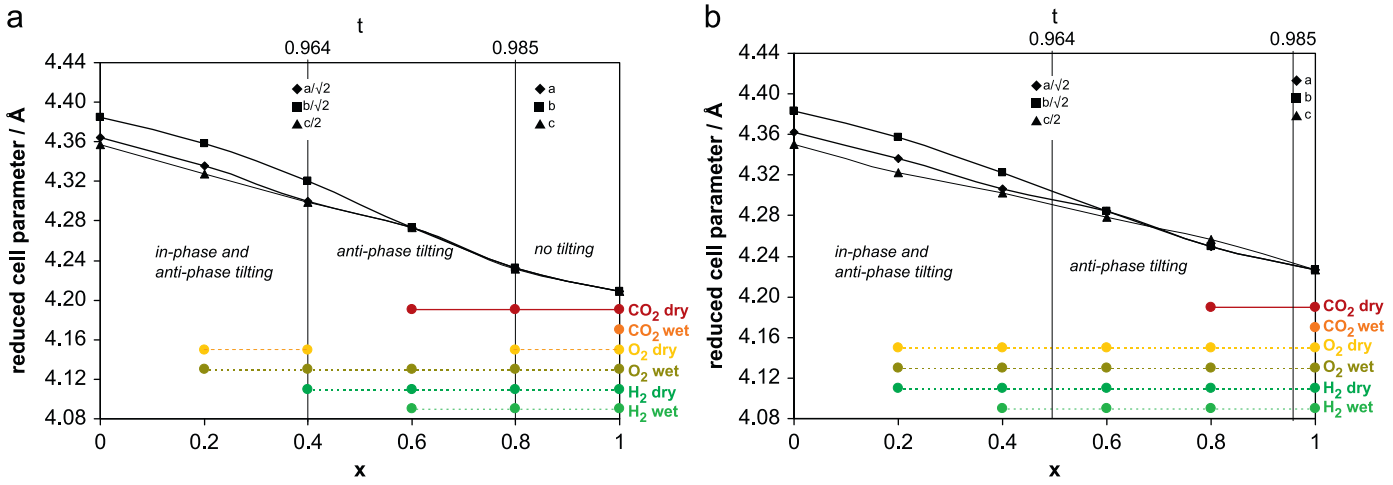

Fig. 3. Reduced unit-cell parameter as a function of composition, superimposed with stability information under different atmospheres for (a) $Ba(Pr_{1-x}Zr_x)_{0.9}Y_{0.1}O_{3-\delta}$ and (b) $Ba(Pr_{1-x}Zr_x)_{0.8}Y_{0.2}O_{3-\delta}$. Stability was analysed by X-ray diffraction analysis after heat treatment at 600 °C. Bullet points signify stable compositions for each atmosphere.

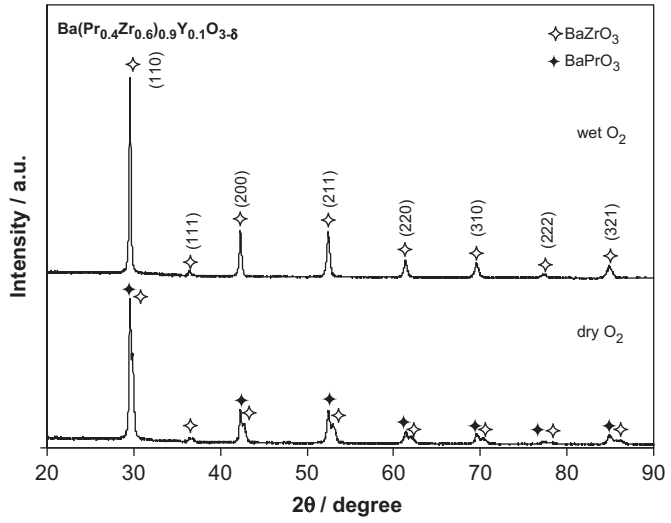

Fig. 4. X-ray diffraction patterns of composition $Ba(Pr_{1-x}Zr_x)_{0.9}Y_{0.1}O_{3-\delta}$, $x=0.6$, after annealing at 600 °C in dry and wet O_2 atmospheres, highlighting instability in dry O_2. Filled and open stars indicate perovskite phases of differing lattice parameter.

$BaPr_{0.7}Gd_{0.3}O_{3-\delta}$ in wet oxygen [5], could not be observed for the current Y-containing systems. In both wet and dry oxygen, stability is shown to be improved with increase in the Zr content. This observation concurs well with the increase in the tolerance factor [25], and associated increase in symmetry with increase in the Zr-content summarised in Fig. 3. Interestingly, the intermediate composition $Ba(Pr_{0.4}Zr_{0.6})_{0.9}Y_{0.1}O_{3-\delta}$ decomposes into two perovskite phases of differing lattice parameters on annealing in dry oxygen (Fig. 4). Note that a $BaZrO_3$-based perovskite is probably the minority phase, while the positions of the reflections of the main phase are still relatively close to corresponding reflections of the single-phase composition retained in wet O_2; this suggests that the prevailing phase might still be a mixed $Ba(Pr_{1-x}Zr_x)_{1-y}Y_yO_{3-\delta}$ composition.

3.3.2. 10%H_2/N_2

Magrasó et al. [12] performed TGA analysis in wet and dry 5% H_2 and documented substantial decomposition of the $BaZr_xPr_{0.7-x}Gd_{0.3}O_{3-\delta}$ system in the temperature range 450–650 °C for compositions with values of $x<0.5$. Hence, in the current work, stability was assessed after annealing for 5 h at a similar temperature (600 °C) on subsequent examination by XRD (Fig. 3a and b). For $BaPr_{1-y}Y_yO_{3-\delta}$ samples, decomposition was observed in both systems ($y=0.1$ and $y=0.2$) leading to the formation of a reduced $BaPr_2O_4$-based phase under dry conditions or $Pr(OH)_3$ under wet conditions with some $BaCO_3$ due to rapid reaction between $Ba(OH)_2$ and CO_2. These observations are consistent with the work of Magrasó et al.[12]. One may describe the formation of secondary phases as follows:

$$Ba(Pr,Y)O_{3-\delta}+xH_2 \rightarrow xBa(Pr,Y)_2O_4+xBa(OH)_2+(1-2x)Ba(Pr,Y)O_{3-\delta} \quad (2)$$

for dry conditions, or:

$$Ba(Pr,Y)O_{3-\delta}+0.5xH_2+2xH_2O \rightarrow xPr(OH)_3+xBa(OH)_2 +(1-x)Ba(Pr,Y)O_{3-\delta} \quad (3)$$

for wet conditions, followed by ready conversion of barium hydroxide in the presence of atmospheric CO_2:

$$xCO_2+xBa(OH)_2 \rightarrow xBaCO_3+xH_2O \quad (4)$$

For low Zr-contents in the system $Ba(Pr_{1-x}Zr_x)_{1-y}Y_yO_{3-\delta}$, decomposition is generally manifested by the presence of $BaCO_3$ and splitting of the perovskite reflections, Fig. 5. Nevertheless, the composition, $Ba(Pr_{0.8}Zr_{0.2})_{0.8}Y_{0.2}O_{3-\delta}$, containing large quantities of Pr, is stable under dry hydrogen, Fig. 5. Hence, in comparison to the work of Magrasó et al. [12], the present study shows that reduction of the average *B*-site ionic radius, by exchange of Gd^{3+} for the smaller ion Y^{3+}, can substantially extend stability under reducing atmospheres to samples of higher Pr-content. Furthermore, the current work provides the additional information that stability is greater in dry reducing conditions and is retained to a higher Pr content (lower x) in the system with the greatest Y-content, $Ba(Pr_{1-x}Zr_x)_{0.8}Y_{0.2}O_{3-\delta}$ (Figs. 3 and 5). The latter phenomenon can possibly be explained with reference to Fig. 6, which plots the expected tolerance factor with respect to the ionic size of praseodymium in different oxidation states. The formation of the decomposition product $BaPr_2O_4$ in dry 10% H_2/N_2 clearly indicates reduction of Pr^{4+}–Pr^{3+} in this atmosphere. When Pr is in the 3+ oxidation state, the expected trends in tolerance factor of the two systems cross at approximately $x=0.4$ (Fig. 6). Hence, at low values of x, the compositions with highest tolerance factor will be those with the higher Y-content, i.e. $Ba(Pr_{1-x}Zr_x)_{0.8}Y_{0.2}O_{3-\delta}$, This is in agreement with the observed experimental data in Figs. 3 and 5 on annealing in 10% H_2/N_2; thus, it appears to

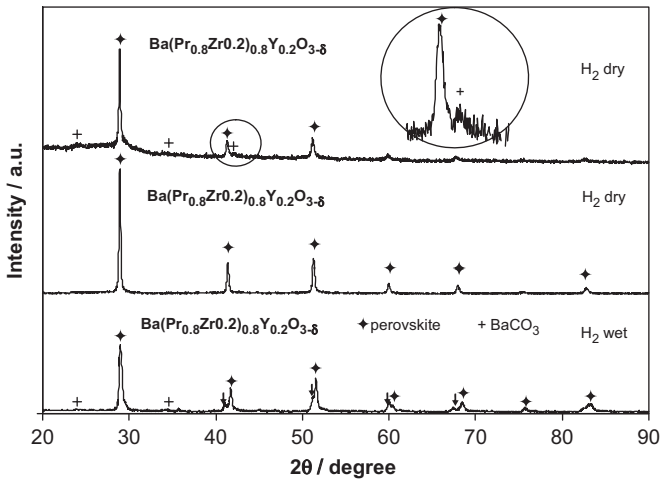

Fig. 5. X-ray diffraction patterns of compositions from the systems $Ba(Pr_{1-x}Zr_x)_{0.9}Y_{0.1}O_{3-\delta}$ and $Ba(Pr_{1-x}Zr_x)_{0.8}Y_{0.2}O_{3-\delta}$ with $x=0.2$, after annealing at 600 °C in wet and dry H_2 atmospheres, highlighting greater stability in the system with higher Y-content and greater stabilities in dry atmospheres.

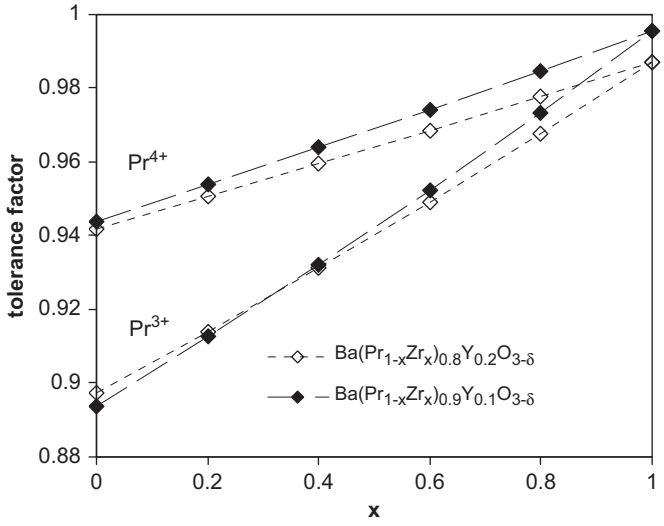

Fig. 6. Expected trends in tolerance factor with respect to the ionic size of praseodymium in different oxidation states for the $Ba(Pr_{1-x}Zr_x)_{0.9}Y_{0.1}O_{3-\delta}$ and $Ba(Pr_{1-x}Zr_x)_{0.8}Y_{0.2}O_{3-\delta}$ systems.

be possible to predict the observed stability even in reducing conditions from simple tolerance factor calculations on consideration of the reduction of Pr and its associated increase in ionic size.

3.3.3. *Pure CO_2*

The stability of the systems in flowing dry CO_2 measured by TGA is shown in Fig. 7. Major weight gains can be observed for both systems for compositions of low Zr-content above 500 °C and the total weight gain increases with decrease in the Zr-content. The uptake of CO_2 occurs in two stages, a low-temperature stage corresponding to minor weight gain followed by a dominant high-temperature regime in which the majority of the weight gain takes place. This behaviour resembles that reported for the $BaZr_xPr_{0.7-x}Gd_{0.3}O_{3-d}$ [12] and $BaCe_{1-x}R_xO_{3-\delta}$ systems [26]. In general, the onset temperature of the low- and high-temperature ranges increases with increasing Zr-content, reflecting an increased stability associated with increase in tolerance factor and symmetry, and lower basicity of the *B*-site cation (Fig. 3, [25]). With increase in the Zr-content, second-stage carbonation is observed to occur over wider temperature ranges, suggesting slower carbonation kinetics or gradual evolution towards the upper temperature limit of the carbonation range, as indicated by thermodynamic calculations in Section 4. For samples of high Pr-content, the presence of maxima in weight gain can be observed followed by weight loss at the highest temperatures. This phenomenon is analogous to the carbonation behaviour of $BaCeO_3$ reported by Zakowsky et al. [26] who demonstrated that the formed $BaCO_3$ decomposes at high temperatures with reformation of the perovskite phase. It is interesting to note that the location of these maxima shifts to higher temperatures with increase in the Zr-content, reflecting a higher stability of $BaZrO_3$ than $BaCeO_3$, in agreement with the corresponding thermodynamic predictions [27].

Post-mortem analysis of powdered samples by XRD after high temperature carbonation showed the presence of the component oxides and barium carbonate. In Fig. 8, the maximum CO_2 uptake on second stage carbonation is compared with the theoretical value calculated for the stoichiometric formation of $BaCO_3$. Fig. 8 shows an approximately linear, inverse relationship between the value of x and the extent of carbonation and higher carbonation in the system with the highest Y-content. Note that this is the opposite dependence to that observed in more reducing conditions, in Section 3.3.2, in agreement with tolerance factor considerations outlined in Fig. 6. These predictions of

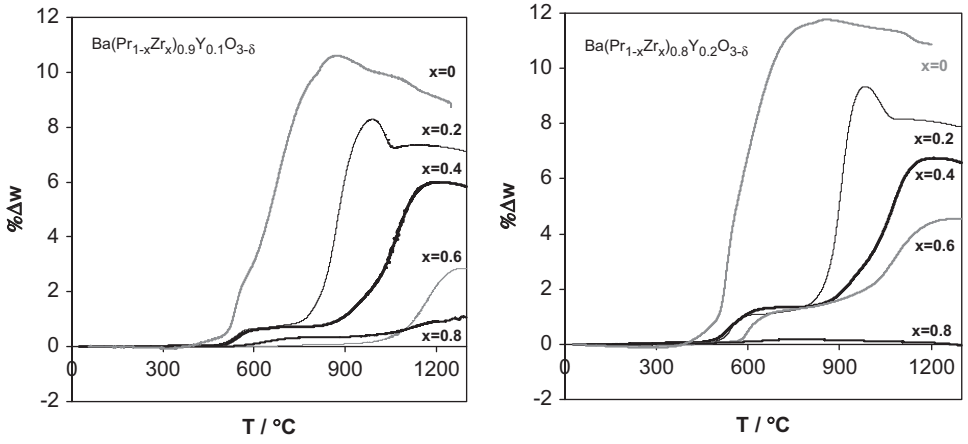

Fig. 7. TGA plot for the $Ba(Pr_{1-x}Zr_x)_{0.9}Y_{0.1}O_{3-\delta}$ and $Ba(Pr_{1-x}Zr_x)_{0.8}Y_{0.2}O_{3-\delta}$ systems heated under dry, flowing 100% CO_2 at a rate of 1 °C/min.

carbonation may even be somewhat underestimated due to a counter effect of weight losses by gradual reduction of Pr^{4+} to Pr^{3+}. If one assumes close to 50% conversion to Pr^{3+} one obtains up to about 93% carbonation for $BaPr_{0.8}Y_{0.2}O_{3-\delta}$ and about 87% for $BaPr_{0.9}Y_{0.1}O_{3-\delta}$.

Zakowsky et al. [26] suggested that the low-temperature stage could be due to carbonation of exolved BaO following formation of a Ba-deficient phase during sample preparation. Alternatively, it may be that the low-temperature regime is related to surface carbonation, while the second stage, corresponding to bulk carbonation, would be displaced to higher temperatures due to kinetic limitations. In order to assess the low-temperature stage more fully, subsequent XRD analysis was performed on samples annealed at 600 °C for 12 h under dry CO_2. The results, summarised in Fig. 3a and b, show the stability limit at 600 °C to be wider in $Ba(Pr_{1-x}Zr_x)_{0.9}Y_{0.1}O_{3-\delta}$ ($x \geq 0.6$) than in the system $Ba(Pr_{1-x}Zr_x)_{0.8}Y_{0.2}O_{3-\delta}$ ($x \geq 0.8$). To highlight this point, Fig. 9 plots the intensity ratio between the most intense (111) reflection in the $BaCO_3$ phase and the most intense (110) reflection in the perovskite phase for samples carbonated at 600 °C for 12 h in wet and dry atmospheres. This intensity ratio allows an estimation of variations in the relative amounts of the perovskite and $BaCO_3$ phases with changes in composition. Fig. 9 shows that the amount of first stage carbonation is greater with decrease in the Zr-content and greater in the system with the highest Y-content. Hence, the extents of both low temperature and high temperature carbonation have the same tendencies, reinforcing the relationship between stability, increased tolerance factor, crystallographic symmetry, and basicity. Another important observation is that much greater carbonation occurs in a wet rather than a dry atmosphere. This phenomenon will be discussed in the following section. The corresponding diffraction patterns for low temperature carbonation, in compositions with values of $x \geq 0.2$ up to the stability limit for each system, show predominantly the perovskite phase with the additional presence of $BaCO_3$. In contrast, significant decomposition is observed for the Zr-free samples at this temperature, with formation of the component oxides and $BaCO_3$ accompanied by substantial decrease in the relative XRD peak intensities of the perovskite phase.

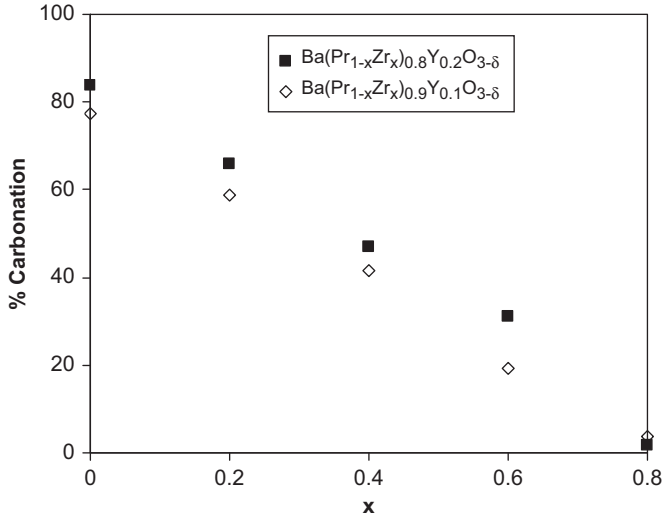

Fig. 8. Comparison of the maximum CO_2 uptake on second stage carbonation in dry flowing CO_2 with the theoretical value calculated for the stoichiometric formation of $BaCO_3$ for each composition for the systems $Ba(Pr_{1-x}Zr_x)_{0.9}Y_{0.1}O_{3-\delta}$ and $Ba(Pr_{1-x}Zr_x)_{0.8}Y_{0.2}O_{3-\delta}$.

3.3.4. *Stability in wet compared to dry atmospheres*

Figs. 3, 5, and 9 all suggest that the stability of the title phases is higher in drier conditions for CO_2 and 10% H_2/N_2 atmospheres. Water has been suggested to have a reducing effect in $BaPrO_3$, and to lead to hydration of Ba^{2+} and Pr^{4+} to form $Ba(OH)_2$ and $Pr(OH)_3$ [5,12]:

$$BaPrO_3 + 2.5H_2O \rightarrow Pr(OH)_3 + Ba(OH)_2 + 1/2O_2 \quad (5)$$

It should be noted that this decomposition reaction occurs even in wet oxygen for compositions such as $BaPr_{0.7}Gd_{0.3}O_{3-\delta}$ which contains a large average *B*-site cation radius [5]. One can envisage that reduction of Pr will lead to substantial increases in average *B*-site cation radius; hence, complete or partial decomposition may be considered likely to occur in wet reducing atmospheres with the formation of the parent hydroxides, even in the title materials.

4. Thermodynamic guidelines

Thermodynamic predictions for spontaneous carbonation of barium zirconate may be based on the Gibbs free energy of reaction (6):

$$BaZrO_3(s) + CO_2 \leftrightarrow BaCO_3(s) + ZrO_2(s) \quad (6)$$

This is dependent on working conditions, namely temperature, pressure, and atmospheric composition, which also determines the carbon dioxide partial pressure pCO'_2. For prospective firing and operation of the actual ceramic materials, one expects conditions close to normal pressure (1 atm), and equilibrium is

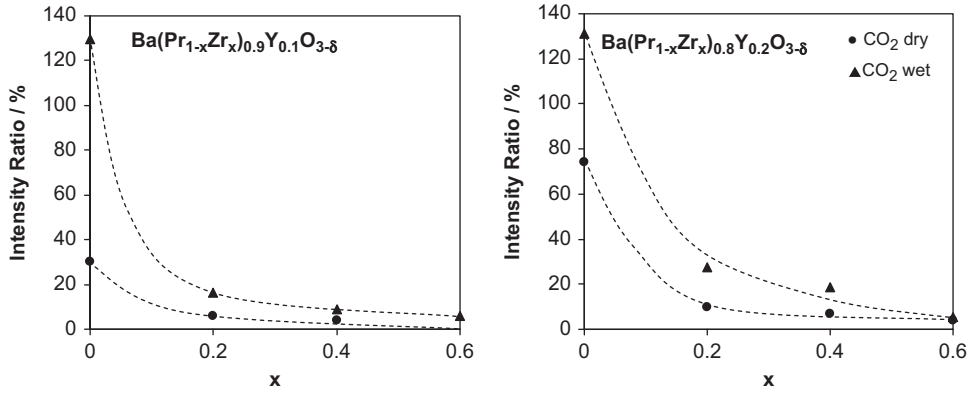

Fig. 9. The XRD intensity ratio between the most intense (111) reflection of the $BaCO_3$ phase and the most intense (110) reflection in the perovskite phase for samples carbonated at 600 °C for 12 h in wet and dry atmospheres for the systems $Ba(Pr_{1-x}Zr_x)_{0.9}Y_{0.1}O_{3-\delta}$ and $Ba(Pr_{1-x}Zr_x)_{0.8}Y_{0.2}O_{3-\delta}$, corresponding to first stage carbonation.

dictated by the temperature dependence of Gibbs free energy and the relevant relation between mass action constant and partial pressure

$$K_{eq} = RT\ln(pCO'_2) = \Delta G_1(T) \quad (7)$$

In this case, the Gibbs free energy calculations may be based on the relevant thermodynamic data (e.g. Refs. [28,29]). Indeed, pressured conditions may also be used for less common synthesis methods (e.g. [30]) or in geochemistry [31].

Actually, the Gibbs free energy of reaction 6 is insufficient for a complete thermodynamic analysis of carbonation of barium zirconate. In fact, the equilibrium for coexistence of barium zirconate and barium carbonate may vary on moving from conditions of barium oxide excess to deficiency. These limiting conditions are established by 3-phase reactions, and one expects the onset of ZrO_2 segregation for barium deficiency to correspond to the 3-phase equilibrium described by reaction 6, with the co-existence of solid phases, $BaCO_3$, $BaZrO_3$, and ZrO_2. For barium oxide excess, one expects segregation of Ba_2ZrO_4 as a secondary phase [27], and the 3-phase equilibrium for $BaCO_3$, $BaZrO_3$ and Ba_2ZrO_4 can be given by

$$Ba_2ZrO_4(s) + CO_2 \leftrightarrow BaCO_3(s) + BaZrO_3(s) \quad (8)$$

yielding the corresponding equilibrium condition

$$\ln(pCO''_2) = \Delta G_2/(RT) \quad (9)$$

Thus, upper and lower limits for equilibrium between the perovskite and carbonate phases are given by Eqs. 7 and 9. Fig. 10 shows that these limiting conditions differ by orders of magnitude in partial pressure at identical temperatures; equally, major changes in temperature are required to avoid carbonation.

One can also extend the thermodynamic analysis for the case of a gradual change from barium excess to barium deficiency, and to predict other relevant thermodynamic features for the simplest $BaO–ZrO_2–CO_2$ system. Equilibrium conditions along the $BaZrO_3$/$BaCO_3$ two-phase boundary can be described as a function of the activity ratio of component oxides as follows:

$$0.5BaO + 0.5BaZrO_3 + CO_2 \leftrightarrow BaCO_3 + 0.5ZrO_2 \quad (10)$$

The corresponding equilibrium constant then yields the interdependence between temperature, CO_2 partial pressure, and a_{BaO}:a_{MO2} activity ratio:

$$\log(pCO_2) + 0.5\log(a_{BaO}/a_{ZrO_2}) = \Delta G_3/(2.303RT) \quad (11)$$

Similarly, corresponding thermodynamic relations for the dependence of carbon dioxide partial pressure and/or activity ratio on temperature for other two-phase equilibria can be derived and equilibrium diagrams constructed on combining the complete set of relevant 2-phase equilibria. The equilibrium diagram for pure dry CO_2 (Fig. 11) clearly shows that barium zirconate with slight barium excess is prone to carbonation in CO_2-rich atmospheres even for temperatures as high as 900 °C, i.e., well above prospective operation temperatures; this limiting condition is shown as T_{up}. Nevertheless, tolerance to CO_2 is significantly enhanced by lowering the activity ratio, even without reaching the onset of ZrO_2 as secondary phase, at the lowest temperature (T_L).

On assuming that barium zirconate is cooled very slowly, one expects the onset of carbonation at T_{up}, and then gradual carbonation on cooling along the trajectory from T_{up} towards T_L. Thus, carbonation of barium zirconate can only be prevented by slow kinetics, namely by relatively fast cooling to sufficiently low temperatures, in order to attain $BaZrO_3$ in a metastable state. On suppressing barium excess and with a sufficient level of barium oxide deficiency, one expects cooling along the $BaZrO_3/ZrO_2$ boundary, with true thermodynamic inhibition of carbonation for temperatures down to about 450 °C. This lower temperature limit for the $BaZrO_3/BaCO_3$ equilibrium (T_L) is also more likely to contribute to kinetic inhibition.

The chemical potential gradient for carbonation in contact with a pure CO_2 atmosphere can be expressed as $\Delta\mu = RT\ln(1/pCO_2)$. Thus, the scale in Fig. 10 is a measure of relative chemical potential difference $\Delta\mu/(2.3RT) = -\log(pCO_2)$, and can be used as a guideline for changes in thermodynamic driving-force for carbonation. As long as one expects excess of barium oxide, the thermodynamic driving-force for carbonation in isothermal conditions should remain at the interception between the upper temperature line (T_{up}) and a vertical line for the actual temperature. This driving-force will decrease on exhausting the excess of barium oxide, thus moving equilibrium conditions

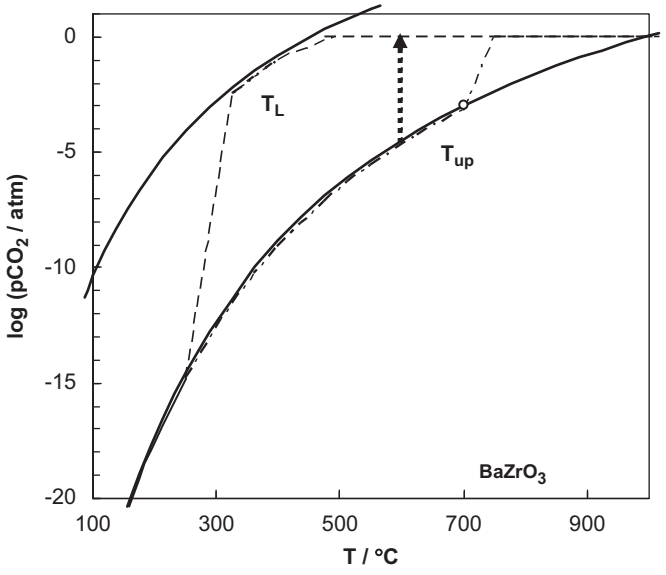

Fig. 10. Thermodynamic predictions of lower and upper limiting conditions for decomposition of $BaZrO_3$ with barium oxide excess and deficiency.

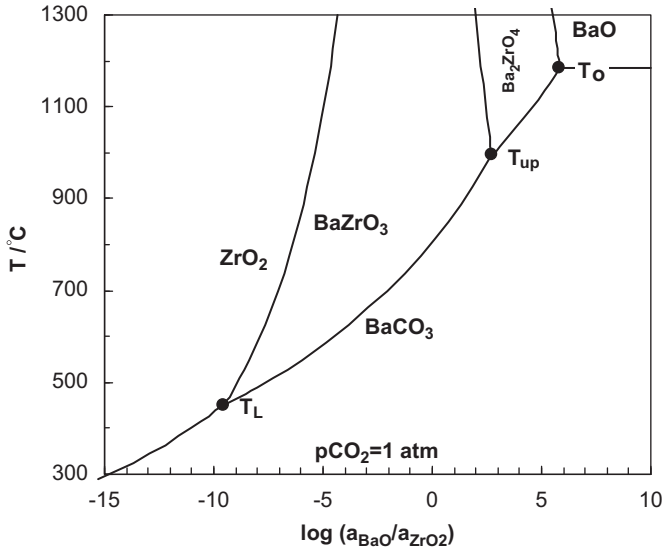

Fig. 11. Predicted equilibrium diagram for the $BaO–ZrO_2–CO_2$ system at $pCO_2 = 1$ atm.

upwards in the pCO_2 scale. In addition, carbonation may be halted if the equilibrium conditions meet the actual partial pressure in the atmosphere before reaching the lower temperature line (T_L). Therefore, carbonation of barium zirconate at temperatures above about 500 °C will be mainly related to consumption of excess of barium oxide or heterogeneities corresponding to the coexistence of barium oxide-rich and deficient zones.

Interpretation of thermoanalytical results on heating is more complex than the discussed thermodynamic interpretation for carbonation on cooling. The progress of carbonation on heating is dictated by opposite effects exerted by progressively enhancing kinetics and decreasing the thermodynamic driving-force. For example, Fig. 10 shows schematic representations of changes expected for a sample with initial barium oxide excess, on assuming either fast kinetics (dotted line), or relatively slow kinetics (dashed line), thus shifting the onset of significant carbonation to higher temperatures. Note also that $-\log(pCO_2)=\Delta\mu/(2.3RT)$ is a measure of the relative chemical potential difference, thus representing the thermodynamic driving-force for carbonation, which remains high as long as the sample remains in the barium oxide excess condition. On exhausting this excess, the driving-force may drop sharply. Barium carbonate may even start to decompose before reaching the upper decomposition temperature (T_{up}) provided that solid-state kinetics do not hinder reformation of the perovskite, and that it retains barium deficiency. Reformation of the perovskite has, indeed, been reported for $BaCeO_3$ [26].

Fig. 11 also shows that carbonation of pure barium oxide may occur for temperatures up to the reference temperature T_o, for the $BaO/BaCO_3$ equilibrium; this is still significantly above the upper limit of the temperature range for equilibrium between the perovskite phase and barium carbonate (T_{up}). Similar calculations have been performed for a variety of $AO–BO_2–CO_2$ systems, and the corresponding differences between the decomposition temperature at its lowest limit (for deficiency of alkali earth oxide), and highest limit (for alkali earth excess), with respect to the reference temperatures T_o, are presented in Fig. 12. These results can be used as a guideline for assessing the resistance to carbonation of $A^{II}B^{IV}O_3$ perovskites, and to confirm the expected correlation between resistance to carbonation and Goldschmidt tolerance factor. For example, $BaCeO_3$ is more prone to carbonation than $BaZrO_3$, mainly at the barium oxide limit, due to a relatively low tolerance factor.

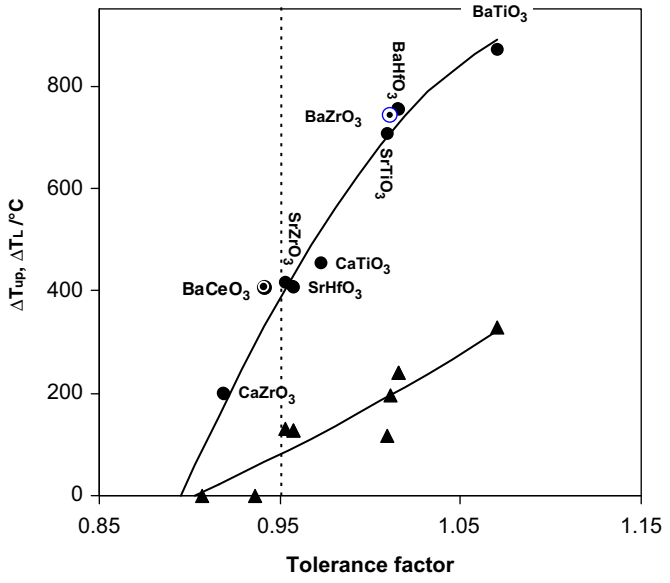

Fig. 12. Dependence of decomposition temperature gaps at the lowest limit ($\Delta T_L=T_L-T_{ref}$) and highest limit ($\Delta T_{up}=T_{up}-T_{ref}$), where the reference temperatures are T_o=694, 937, and 1190 °C for $CaO/CaCO_3$, $SrO/SrCO_3$, and $BaO/BaCO_3$ equilibria, respectively.

The dotted line in Fig. 12 represents the expected location of $BaPrO_3$. In this case, one expects suppression of the lower and upper temperature limits, with respect to T_o, by about ≈ -400 and -70 °C, respectively, and thus $T_L \approx 790$ °C and $T_{up} \approx 1120$ °C, at $pCO_2=1$ atm. This lower limit for $BaPrO_3$ is much higher than that of the corresponding zirconate, thus implying the corresponding increase in thermodynamic driving-force, and anticipates the onset of significant carbonation of $BaPrO_3$ during typical TGA experiments in a CO_2 atmosphere (Fig. 7). The experimentally observed reversion to weight losses before reaching the upper temperature limit T_{up}, Fig. 7, is also consistent with reformation of a barium deficient perovskite, assisting decomposition of barium carbonate.

In addition, kinetics of carbonation may be promoted in wet CO_2 or even wet atmospheres containing relatively low CO_2, as found on studying the performance of CaO in CO_2 capture [32]. Humidity increases the sensitivity of the $Ba(Pr_{1-x}Zr_x)_{1-y}Y_yO_{3-\delta}$ materials to reducing atmospheres. Reduction of Pr^{4+}–Pr^{3+} may also be assisted by the ready incorporation of protonic species as described by the point defect reaction:

$$H_2O+O_O^x+2Pr_B^x \rightarrow 2Pr'_B+2OH_O^{\bullet} \quad (12)$$

This is consistent with the expected decrease in stability of these perovskites upon increasing the fraction of relatively large Pr^{3+} cations, with corresponding excessive deviations from the ideal tolerance factor.

5. Conclusions

Detailed structural analysis of $Ba(Pr_{1-x}Zr_x)_{1-y}Y_yO_{3-\delta}$ materials showed a strong dependence of unit cell volume and lattice distortion on composition in accord with variations in the tolerance factor. Stability was assessed with emphasis on degradation upon exposure to carbon dioxide, and also stability differences between reducing and oxidising atmospheres. Close correlations between the stability under different atmospheres and the tolerance factor were found. Stability ranges of the perovskite phase are significantly lower in wet CO_2 or wet H_2 than for the corresponding dry atmospheres.

Thermodynamic analysis of the $BaO–ZrO_2–CO_2$ system was performed to obtain guidelines for interpretation of the CO_2 resistance of $Ba(Zr,Pr)O_3$-based materials. The analysis demonstrated significant differences between the CO_2 stability for materials with excess and deficiency of alkali earth oxide, which could be accounted for by corresponding upper and lower temperature limits for the perovskite/carbonate equilibrium. On combining thermodynamic calculations for a variety of $A^{II}B^{IV}O_3$ perovskites, a high degree of correlation between the stability limits and the Goldschmidt tolerance factor was demonstrated. The upper and lower temperature limits of $ABO_3/BaCO_3$ equilibria can be used to predict the evolution of carbonation on cooling from high temperatures and also upon re-heating ABO_3 perovskites in CO_2-rich atmospheres, as confirmed by thermogravimetric analysis.

Acknowledgments

This work was supported by the FCT, Portugal (Project PTDC/CTM/66243/2006), the European Commission under Project

STREP033410-MATSILC, Sponsorship by Martifer Energia, and the MICINN (Project no. ENE2009-14750-C05-03).

References

[1] L. Li, J.R. Wu, M. Knight, S.M. Haile, Electrochem. Soc. Proc. 28 (2001) 58.
[2] S. Mimuro, S. Shibako, Y. Oyama, K. Kobayashi, T. Higuchi, S. Shin, S. Yamaguchi, Solid State Ionics 178 (2007) 641.
[3] T. Fukuia, S. Oharaa, S. Kawatsu, Solid State Ionics 116 (1999) 331–337.
[4] K.A. Furøy, R. Haugsrud, M. Hänsel, A. Magrasó, T. Norby, Solid State Ionics 178 (2007) 461.
[5] A. Magrasó, F. Espiell, M. Segarra, J.T.S. Irvine, J. Power Sources 169 (2007) 53.
[6] A. Magrasó, R. Haaugsrud, M. Segarra, T. Norby, J. Electroceram. 23 (2009) 80.
[7] V.P. Gorelov, B.L. Kuzin, V.B. Balakireva, N.V. Sharova, G.K. Vdovin, S.M. Beresnev, Yu.N. Kleshchev, V.P. Brusentsov, Russ. J. Electrochem. 37 (5) (2001) 505.
[8] C.S. Knee, A. Magrasó, T. Norby, R.I. Smith, J. Mater. Chem. 19 (2009) 3238.
[9] N. Bonanos, K.S. Knight, B. Ellis, Solid State Ionics 79 (1995) 161.
[10] F. Chen, O. Toft Sørensen, G. Menga, D. Penga, J. Mater. Chem. 7 (3) (1997) 481.
[11] C. Zuo, S. Zha, M. Liu, M. Hatano, M. Uchiyama., Adv. Mater. 18 (2006) 3318.
[12] A. Magrasó, X. Solans, J.T.S. Irvine, M. Segarra, Ceram. Int. 35 (2009) 1819.
[13] S.V. Bhide, A.V. Virkar, J. Electrochem. Soc. 146 (12) (1999) 4386.
[14] J. Rodriguez-Carvajal, Satellite Meeting on Powder Diffraction, in: Abstracts of the 15th Conference of the International Centre for Diffraction Data, Toulouse, 1990.
[15] I. Antunes, F.M. Figueiredo, J.R. Frade, J. Gracio, D.P. Fagg, J. Solid State Chem. 182 (8) (2009) 2149.
[16] W.T. Fu, D. Visser, D.J.W. IJdo, J. Solid State Chem. 165 (2002) 393.
[17] C.J. Howard, K.S. Knight, B.J. Kennedy, E.H. Kisi, J. Phys.: Condens. Mater. 12 (2000) L677.
[18] K.S. Knight, Solid State Ionics 145 (2001) 275.
[19] H.D. Megaw, Crystal Structures—A Working Approach, W.B. Saunders, Philadelphia, 1973.
[20] I.M. Reaney, E.L. Colla, N. Setter, Jpn. J. Appl. Phys. 33 (1994) 3984.
[21] D.I. Woodward, I.M. Reaney, Acta Crystallogr. B 61 (2005) 387.
[22] C.J. Howard, H.T. Stokes, Acta Crystallogr. B 54 (1998) 782.
[23] A.M. Glazer, Acta Crystallogr. B 28 (1972) 3384.
[24] R.D. Shannon, Acta Crystallogr. A 32 (1976) 751.
[25] K.D. Kreuer, Solid State Ionics 97 (1997) 1.
[26] N. Zakowsky, S. Williamson, J.T.S. Irvine, Solid State Ionics 176 (2005) 3019.
[27] A. Brandão, J.F. Monteiro, A.V. Kovalevsky, D.P. Fagg, V.V. Kharton, J.R. Frade, Solid State Ionics, 10.1016/j.ssi.2010.02.006.
[28] H. Yokokawa, T. Kawada, M. Dokiya, J. Am. Ceram. Soc. 72 (1989) 152.
[29] H. Yokokawa, N. Sakai, T. Kawada, M. Dokiya, J. Solid State Chem. 94 (1991) 106.
[30] M.M. Lencka, R.E. Riman, Chem. Mater. 5 (1993) 61.
[31] P.M. Wang, A. Anderko, R.D. Springer, D. Ronald, J.J. Kosinski, M.M. Lencka, M. Malgorzata, J. Geochem. Exp. 106 (2010) 219.
[32] F. Zeman, Int. J. Greenhouse Gas Control 2 (2008) 203.